Check for updates

Analyst

Accepted Manuscript

This article can be cited before page numbers have been issued, to do this please use: T. Zheng, W. Adi, P. Campagnola and F. Yesilkoy, *Analyst*, 2026, DOI: 10.1039/D6AN00137H.

Volume 143
Number 10
21 May 2018
Pages 2185-2436

Analyst

rsc.li/analyst

ISSN 0003-2654

ROYAL SOCIETY OF CHEMISTRY

PAPER
Huinan Yang, Chengxing Shen, Xiaoshu Cai *et al.*
Noninvasive and prospective diagnosis of coronary heart disease with urine using surface-enhanced Raman spectroscopy

This is an Accepted Manuscript, which has been through the Royal Society of Chemistry peer review process and has been accepted for publication.

Accepted Manuscripts are published online shortly after acceptance, before technical editing, formatting and proof reading. Using this free service, authors can make their results available to the community, in citable form, before we publish the edited article. We will replace this Accepted Manuscript with the edited and formatted Advance Article as soon as it is available.

You can find more information about Accepted Manuscripts in the Information for Authors.

Please note that technical editing may introduce minor changes to the text and/or graphics, which may alter content. The journal's standard Terms & Conditions and the Ethical guidelines still apply. In no event shall the Royal Society of Chemistry be held responsible for any errors or omissions in this Accepted Manuscript or any consequences arising from the use of any information it contains.

ROYAL SOCIETY OF CHEMISTRY

rsc.li/analyst

View Article Online
DOI: 10.1039/D6AN00137H

Fix or Freeze? Spectral Differences Arising from Tissue Preparation in Chemical Imaging

Tianyi Zheng[1], Wihan Adi[1], Paul J Campagnola[1], Filiz Yesilkoy[1*]
[1]Department of Biomedical Engineering, University of Wisconsin-Madison, Madison, WI, USA
[*]Corresponding author: filiz.yesilkoy@wisc.edu.

Abstract

Spectrochemical imaging has emerged as a powerful, label-free modality for visualizing the biochemical composition of tissues based on intrinsic vibrational signatures. Specifically, mid-infrared spectrochemical imaging (MIRSI) is becoming essential for fundamental biomedical research studying disease mechanisms, identifying biomarkers, and guiding drug development. However, the sensitivity of MIRSI to sample preparation protocols and its impact on spectral data interpretation remain poorly characterized. Here, we systematically compared spectral data collected from rat kidney and liver tissues prepared using standard fresh frozen (FF) and formalin-fixed, paraffin-embedded (FFPE) tissue processing methods using quantum cascade laser (QCL)–based MIRSI. We applied frequently used spectral data processing techniques, including uniform manifold approximation and projection (UMAP), correlation matrices, and second-derivative spectral analysis to characterize preparation-induced differences. FF samples preserved a broader range of biochemical signals, retaining the innate chemical composition of tissues, while FFPE tissues showed reduced spectral diversity and absorption signal intensity. Moreover, we observed a consistent spectral band at 1026 cm^{-1} primarily in FFPE samples, likely arising from fixation-induced chemical modifications and/or structural rearrangements. Our findings demonstrate that tissue preparation substantially alters chemical and morphological information captured by MIRSI, necessitating careful consideration of processing protocols in workflows involving chemical imaging and Artificial Intelligence (AI) - based spectral analysis.

Introduction

Chemical imaging techniques are emerging as powerful analytical methods for tissue analysis in biomedical sciences. Specifically, mid-infrared spectrochemical imaging (MIRSI) is becoming essential for fundamental biomedical research studying disease mechanisms, identifying biomarkers, and guiding drug development [1–3]. Recent advances in mid-infrared (mid-IR) photonics have improved the standard MIRSI instrumentation, such as Fourier transform IR (FTIR) spectrometers[4,5], while introducing new spectrochemical imaging modalities, including dual-frequency combs[6], quantum cascade laser (QCL)-based microscopes[7,8] and optical photothermal IR (O-PTIR) imaging[9]. These MIRSI modalities provide spatially resolved molecular information in *ex vivo* tissue and cell investigations, revealing biological insights beyond the capabilities of optical imaging methods requiring contrast-generating agents. Unlike traditional histological methods that reveal information on structural and morphological features of tissues, chemical imaging captures molecular fingerprints imprinted in optical spectra that reveal the underlying biochemical differences in healthy and diseased tissues[10–12].

The extent of information these techniques can provide in biomedical research and clinical settings depends on the preservation of intrinsic chemical signals. The mid-IR molecular fingerprint spectrum includes key vibrational bands, such as the amide I and II bands (~1650 and ~1550 cm^{-1}) that carry information on proteins' secondary structures, the lipid-associated bands (~1700-1740 cm^{-1}), and phosphoric acid or carbohydrate modes below 1400 cm^{-1}, which can be

View Article Online
DOI: 10.1039/D6AN00137H

used as biomarkers of functional and metabolic cell states. However, these spectral features are potentially sensitive to sample preparation protocols and can be masked or modified if the biochemical integrity of the tissue is compromised[13].

Two widely used preparation methods, fresh frozen (FF) and formalin-fixed, paraffin-embedded (FFPE), offer complementary strengths for different types of applications. FFPE ensures long-term preservation and maintains tissue morphology but induces chemical alterations through protein crosslinking and solvent-based dehydration[14-16]. In contrast, FF tissue preservation protocols better retain labile biomolecules but present logistical challenges related to storage, biosafety and handling[17]. Previously, FTIR spectra from FF tissues were compared to those from FFPE and deparaffinized tissues, revealing spectral changes associated with the tissue preparation processes[18-20]. Similarly, comparative studies using Raman spectroscopy of dewaxed-FFPE and FF tissues from both cancerous and healthy samples reported decreased spectral signal intensity in FFPE samples[21]. However, these earlier studies primarily relied on ensemble-averaged spectra or limited-area measurements, which do not fully capture the pixel-level spectral heterogeneity available in hyperspectral chemical imaging datasets. In contrast, QCL-based MIRSI enables large-scale pixel-resolved analysis across tissue regions, making it possible to evaluate not only mean spectral differences but also band occurrence, ROI-to-ROI variability, and the preservation of spectral information relevant to downstream classification. Consequently, the effects of tissue preparation protocols on spectral datasets were observed but undermined, hindering the reliable interpretability and reproducibility of chemical imaging approaches across different biomedical research and clinical applications[22].

In this study, we investigate how sample preparation methods influence pixel-resolved spectral fidelity, spectral diversity, and downstream data interpretability in QCL-based MIRSI of tissue sections. By analyzing thousands of spectra from rat kidney and liver tissues prepared using standard FF and FFPE protocols, we show that FFPE processing causes significant spectral degradation, including attenuation or disappearance of spectral bands associated with functional biomolecules, such as lipids, nucleic acids, and proteins. Moreover, our second-derivative spectral analysis revealed decreased spectral band diversity in FFPE tissues. In addition, we observed a consistent spectral band at 1026 cm^{-1} primarily in FFPE samples, likely arising from fixation-induced chemical modifications and/or structural rearrangements. To assess whether MIRSI spectra could be used to distinguish tissue types and preparation methods, we applied UMAP for unsupervised clustering, revealing that FF tissue spectra maintained biochemical diversity sufficient for tissue classification, while spectra from FFPE tissues formed a compressed cluster. Logistic regression on UMAP-projected data further revealed that discriminative features between FF and FFPE samples primarily originate from the glycogen and Amide regions. These results emphasize the critical role of tissue preparation in preserving the innate biochemical composition of tissues, highlighting the potential limiting effects of chemical fixing in MIRSI data interpretation using machine learning techniques in chemical imaging pipelines.

Materials and methods

Animal Handling and Tissue Collection

All procedures involving live rats were conducted in accordance with the NIH Guide for the Care and Use of Laboratory Animals and were approved by the Institutional Animal Care and

View Article Online
DOI: 10.1039/D6AN00137H

Use Committee (IACUC) at the University of Wisconsin School of Medicine and Public Health. Adult rats were euthanized via intraperitoneal injection of a mixture containing ketamine (100 mg·kg^{-1}), xylazine (20 mg·kg^{-1}), and acepromazine (3 mg·kg^{-1}), followed by transcardial perfusion with phosphate-buffered saline (PBS) and 4% paraformaldehyde (PFA). Liver and kidney tissues were immediately dissected and divided in half for parallel post-processing by either fresh freezing in OCT or FFPE protocols.

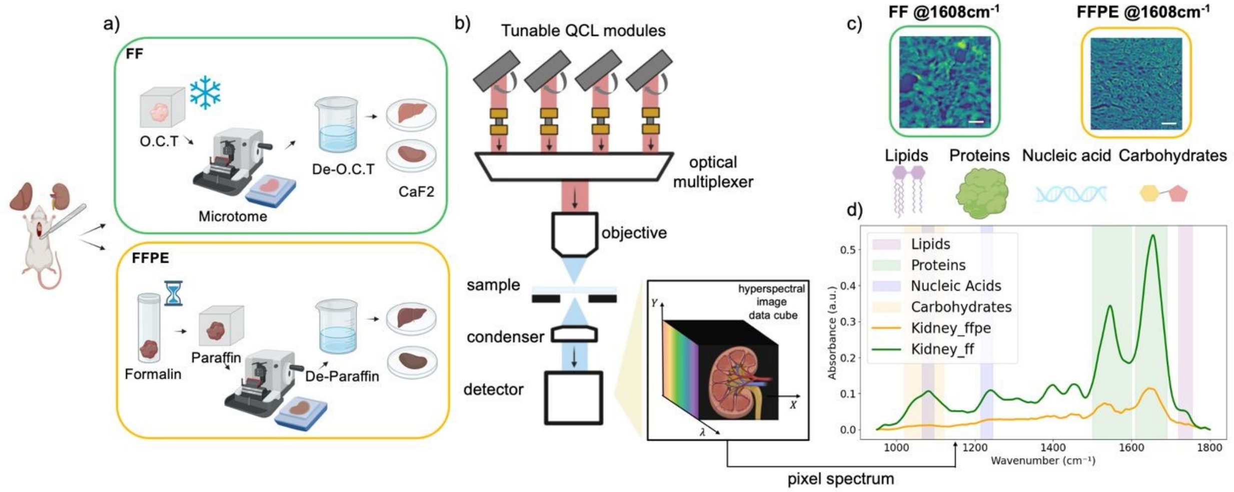

***Figure 1**. **Sample preparation and mid-infrared spectrochemical imaging workflow**. a). Schematic of tissue processing for MIRSI. Rat kidney and liver tissues were prepared either by fresh freezing (FF) in optimal cutting temperature (OCT) compound or formalin fixation followed by paraffin embedding (FFPE). All tissues were sectioned at 10 µm thickness and mounted on CaF$_2$ substrates. Before imaging, the embedding media, OCT or paraffin, were removed. b). Schematic of the QCL-based MIRSI system used for hyperspectral imaging in widefield transmission mode across fingerprint spectral range of 950–1800 cm $^{-1}$. c). Representative mid-IR images of FF and FFPE kidney tissues captured at the Amide I region (1608 cm^{-1}). Scale bars indicate 100 µm. d). Measured absorbance spectra from FF and FFPE kidney tissues. Each spectrum was averaged from ~100,000 pixels. The color bands in the background highlight spectral regions associated with different biomolecules.*

Tissue Embedding and Sectioning

Liver and kidney tissues were prepared using both fresh frozen (FF) and formalin-fixed paraffin-embedded (FFPE) protocols. For FF preparation, tissues were transferred into cryomolds, embedded in optimal cutting temperature (OCT) compound, and snap-frozen on dry ice. Frozen blocks were sectioned at 10 µm thickness using a Leica CM1950 cryostat at −20 °C and mounted onto calcium fluoride (CaF$_2$) substrates. To remove residual OCT, sections were briefly immersed in deionized water (~10–30 s) and subsequently air-dried at room temperature. For FFPE preparation, tissues were first fixed in 10% neutral buffered formalin (NBF) for 24–48 h at room temperature. Following fixation, samples were processed using an automated tissue processor (Sakura VIP5 tissue processor), which performs sequential dehydration in graded ethanol, clearing in xylene, and paraffin infiltration under controlled temperature (typically ~60 °C) and vacuum conditions (overnight cycle). Processed tissues were embedded in paraffin blocks and sectioned at 10 µm thickness using a Leica Histocore Biocut microtome. Sections were mounted onto CaF$_2$ substrates, dried overnight, and briefly incubated at 60 °C to promote adhesion and flattening. Prior to imaging, FFPE sections were deparaffinized using a standardized protocol: two xylene baths (5 min each), followed by two washes in 100% ethanol (5 min each) and one wash in 95% ethanol (5 min). Slides were then rinsed in distilled water and

View Article Online
DOI: 10.1039/D6AN00137H

allowed to air dry completely. All tissue sections were mounted onto pristine calcium fluoride (CaF_2) substrates and stored at 4 °C until spectral imaging.

Quantum Cascade Laser–Based Mid-Infrared Imaging

Mid-infrared hyperspectral imaging was performed using a Spero-QT microscope (Daylight Solutions, Inc.) equipped with four QCL modules, providing spectral coverage from 950 to 1800 cm^{-1} (Figure 1 b), as described in our previous work[23]. High-magnification scans were acquired using a 12.5× infrared objective (NA = 0.7; pixel size = 1.3 μm) and an uncooled microbolometer focal plane array (480 × 480 pixels). All spectral data were collected at a spectral resolution of 2 cm^{-1}. Although 4 cm^{-1} resolution may be sufficient for some applications and may improve acquisition efficiency, the present study used 2 cm^{-1} as a fixed high-resolution setting to sensitively capture subtle preparation-dependent spectral changes.

Preprocessing of Spectrometric Data

After hyperspectral 3D data collection, datasets were processed using custom Python scripts (Figure 2). For each sample type (FF or FFPE liver or kidney; four types in total), ten regions of interest (ROIs) of 0.650 × 0.650 mm^2 (480 × 480 spectra per ROI) were acquired. A total of eight ROIs per sample type were retained for further analysis, yielding 8 × 480 × 480 ~ 1.8 M spectra in total per sample.

Before spectral data preprocessing, we first identified blank pixels, where there is no tissue present, and removed them from the datasets of interest. Those off-tissue pixels in each ROI were identified using Otsu thresholding[24] applied to the mid-IR images collected at the 1608 cm^{-1}, Amide I band, primarily the strongest band in the spectrum. The average of the discarded off-tissue pixels was set as the background spectrum to calculate the noise. Next, we took the second derivative of the background spectrum and calculated its standard deviation (σ), which was then set as the background noise and used to distinguish significant absorption peaks from the background.

From each ROI, 2,000 tissue-associated pixels were randomly selected and saved for further analyses, resulting in a dataset of 16,000 spectra per sample type. Each tissue-associated pixel spectrum was preprocessed by applying a rubberband baseline correction to remove the scattering contributions[25]. For reproducibility, preprocessing and downstream spectral analyses were implemented in custom Python scripts. Tissue-associated regions were identified from the 1608 cm^{-1} image using Otsu-based thresholding, and 2,000 spectra were randomly sampled from each ROI for further analysis. Each extracted spectrum was baseline-corrected using a rubberband algorithm based on convex-hull interpolation to reduce broad background and scattering contributions. For derivative-based peak analysis, spectra were smoothed and differentiated using a Savitzky–Golay filter, and significant peaks were identified using a 3σ threshold estimated from the second derivative of the off-tissue background spectrum. Peak occurrence was evaluated using a ±2 cm^{-1} tolerance window. For classification analysis, spectra were standardized by Z-score normalization prior to PCA, UMAP, and logistic regression.

View Article Online
DOI: 10.1039/D6AN00137H

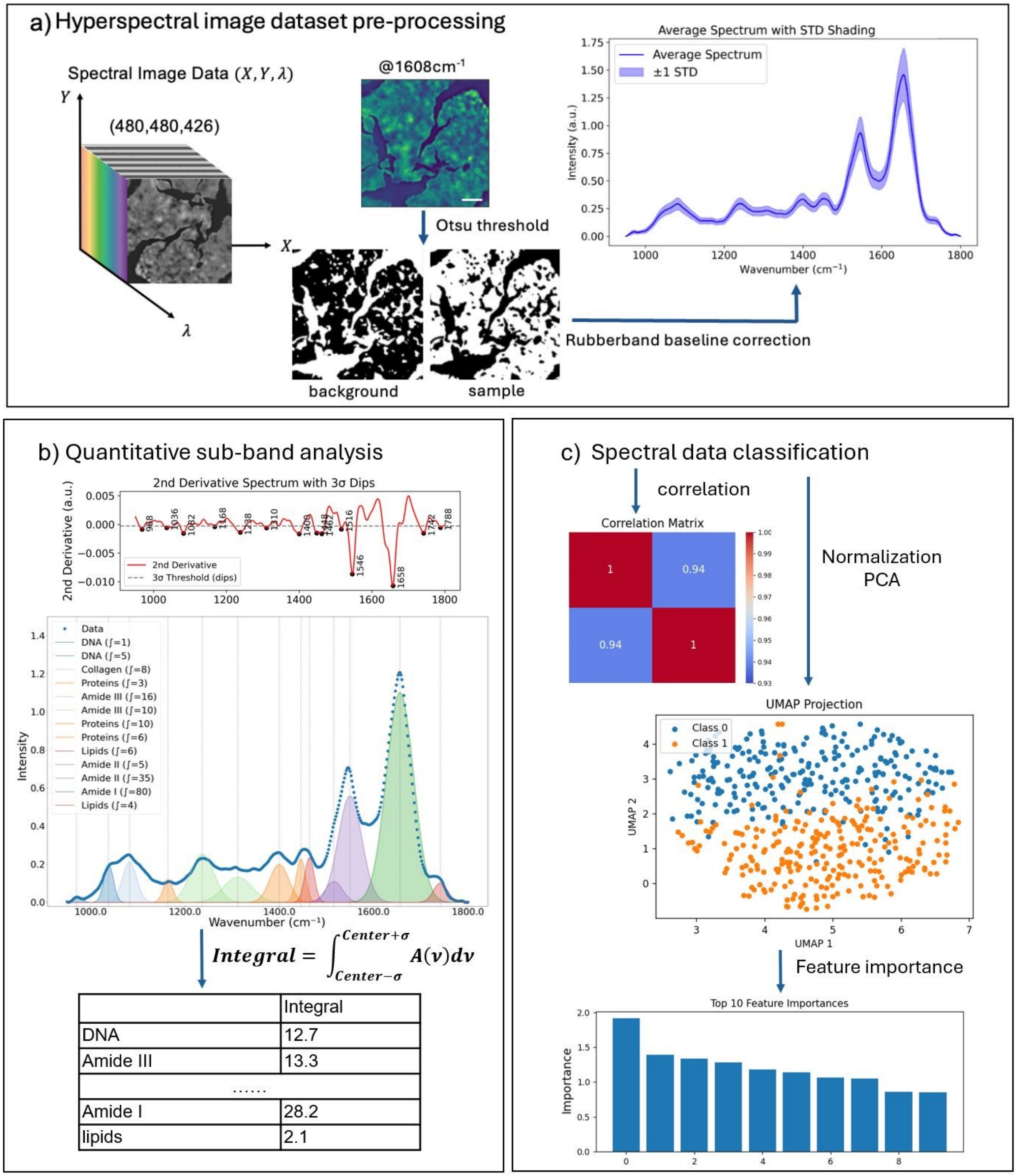

	Integral
DNA	12.7
Amide III	13.3
……	
Amide I	28.2
lipids	2.1

Figure 2. Overview of spectral data processing methods. *a). Eight ROIs were selected from each tissue sample. Tissue-associated sample spectra were extracted by applying Otsu thresholds to a single mid-IR image collected at 1608 cm*$^{-1}$*, Amide I region. Scale bars indicate 100 μm. Next, rubberband baseline correction was applied to the extracted spectra to remove scattering contributions. b). For quantitative sub-band analysis, second-order Savitzky–Golay derivatives were applied to the filtered, polymer-fitted spectral signal. Functional vibrational bands were identified using 3σ rule and quantified using composite Simpson's integration. c). For spectral data classification, correlation heatmaps were generated to illustrate similarities between and within samples. Absorption spectra were Z-score normalized and then subjected to PCA for dimensionality reduction. The processed spectra were classified*

View Article Online
DOI: 10.1039/D6AN00137H

by unsupervised ML methods (UMAP), which was followed by logistic regression to evaluate spectral feature importance.

Quantitative sub-band analysis of spectrometric data

To enhance absorbance band resolution and minimize baseline variations, the second derivative of each absorbance spectrum was computed using a Savitzky–Golay filter[26] (window length = 13, polynomial order = 2; scipy.signal) (Figure 2b). Due to edge effects from filtering, 26 spectral points were trimmed from the original 426-point spectral range. This procedure sharpened overlapping vibrational bands, abundant in complex biological samples, and improved peak detection. From the second-derivative spectra, significant peaks were identified using the 3σ rule, which identifies significant peaks and sub-peaks lying outside the calculated 3σ range[27]. Here, σ was calculated from the discarded off-tissue background spectra, ensuring that peak detection was grounded in statistical rigor rather than an arbitrary threshold.

From each ROI, a subset of 100 pixel-spectra was randomly selected for peak occurrence analysis, and the average spectra were used for sub-band Gaussian fitting (Figure 2b). To quantify the occurrence frequency of specific vibrational bands, peak occurrence was calculated as the number of pixels within each ROI that contains a significant peak (a band passing the 3σ rule) at a spectral position with ± 2 cm^{-1} tolerance. The total occurrence of each vibrational band was then expressed as a count across all analyzed spectra across the ROIs, and the results were plotted as box-and-whisker plots in Figures 3 and 4. This approach reflects how often a characteristic absorbance feature was present among different samples, providing a statistical representation of spectral consistency and biochemical prevalence within the tissue regions.

Quantitative absorbance information for each sub-band was extracted by numerical integration within defined spectral windows using the composite Simpson's rule (scipy.integrate), and vibrational bands were assigned based on established spectral positions of functional groups[28]. The spectral regions used for integration are listed in Table 1.

Spectral data classification

For spectral data classification, a random subset of 2,000 pixel-spectra per ROI (160,000 spectra in total across sample types) was selected. Correlation between ROIs was calculated and displayed in a heatmap, illustrating the degree of similarity within ROIs of the same sample type and highlighting differences across distinct samples. Absorbance spectra were Z-score normalized (mean = 0, standard deviation = 1) for standardization, then subjected to principal component analysis (PCA) for dimensionality reduction, followed by UMAP for visualization of group separation. Finally, feature importance was evaluated using logistic regression, and the top 40 informative wavenumbers were identified (Figure 2c).

View Article Online
DOI: 10.1039/D6AN00137H

Table 1. Reference integration intervals along second-order derivative absorption spectra

Assignment	Peak center [cm^{-1}]	Reference
DNA	~966	29
Glycogen	~1030	30,31
DNA	~1035	32
DNA	~1082	33
Glycogen	~1154	34
Proteins	~1168	35
Amide III	~1238	36
Amide III	~1308	37
Proteins	~1400	38
Proteins	~1448	30
Lipids	~1462	29
Amide II	~1516	39
Amide II	~1546	39
Amide I	~1658	40
Lipids	~1744	37

Results and discussion

Effect of Sample Preparation on Spectral Integrity in Kidney and Liver Tissues

To evaluate the impact of tissue sample preparation on mid-IR spectral datasets, we analyzed rat kidney and liver tissues processed using either FF or FFPE protocols separately (Figures 3, 4). All measured tissues were sectioned at the same nominal thickness of 10 μm following completion of their respective FF or FFPE preparation workflows, ensuring controlled section thickness during microtomy. While minor local variations in effective optical path length may occur due to heterogeneity in tissue structure, these primarily influence overall absorbance intensity rather than spectral features. As demonstrated in Supplementary Fig. S1, the observed spatial heterogeneity within a tissue region is dominated by intensity variations, supporting that thickness effects do not solely drive the spectral feature differences arising from tissue preparation methods reported in this study.

In kidney tissues, FF sections consistently exhibited stronger overall absorption and greater spectral diversity (higher occurrence) compared to FFPE tissues (Figure 3). To support our empirical observations with rigorous data analysis, we considered spectral data from eight ROIs (100 spectra per ROI) per FF and FFPE samples. Based on our 3σ rule, thirteen distinct peaks were consistently observed in FF kidney tissues, with robust preservation of DNA, protein, and lipid-associated bands (Figure 3a). In contrast, only eight bands were detected in FFPE tissues (Figure 3b). Although protein-associated bands (Amide I and II) remained detectable, signals from DNA and lipids were significantly reduced or absent. A weak feature near 1788 cm^{-1} within the carbonyl region was also observed in the spectra; although it could satisfy the detection threshold, it was excluded from further biological interpretation because it could not be confidently interpreted as a robust tissue-associated band.

The spectral differences between FF and FFPE sections were not limited to a uniform reduction in absorbance intensity. Rather, FFPE processing selectively altered the detectability, relative

View Article Online
DOI: 10.1039/D6AN00137H

prominence, and occurrence of specific vibrational bands across the fingerprint region, indicating non-uniform modification of the underlying biochemical information. Importantly, the apparent loss of DNA and lipid associated bands in FFPE tissues should not be interpreted as their complete biochemical absence. Instead, this observation reflects a combination of chemical extraction and reduced spectral detectability under identical analysis conditions. Lipids are known to be partially removed during repeated xylene and ethanol washes during FFPE processing, leading to a reduction in lipid associated vibrational signatures. In contrast, nucleic acids such as DNA and RNA are largely retained within the tissue matrix but undergo chemical modification and crosslinking during formalin fixation, resulting in diminished absorbance intensity and altered band shapes. Because the same processing pipeline were used for both FF and FFPE datasets, the reduced signal amplitude and signal-to-noise ratio in FFPE samples make DNA and RNA associated bands less likely to be detected above threshold, even when present.

The overall diversity of spectral bands was summarized in the occurrence plots in Figure 3a and b for FF and FFPE samples, respectively. Variations in the band occurrence across spectra from eight different ROIs can be attributed to spatial compositional changes across the sectioning cross-section of the kidney, consisting of different tissue and cell types. Moreover, on average, the absorbance of the Amide 1 band in FFPE was 66.3% lower $((Integral_{FF} - Integral_{FFPE})/Integral_{FF})$ than the FF kidney tissue measurements based on our band integral analysis.
We hypothesize that the FFPE protocol is chemically harsh: repeated xylene and ethanol washes can extract or degrade biomolecular components, leading to lower signal intensity and fewer detectable peaks. Similar observations have been reported previously[18-21] using various chemical imaging techniques. In addition to these spectral differences, the representative mid-IR images revealed clear preparation-dependent morphological differences. FF sections frequently exhibited holes, fractures, and discontinuities, whereas FFPE sections appeared more intact and visually uniform. These image-level observations are consistent with the distinct physical consequences of tissue preparation.

To further evaluate whether spatial heterogeneity contributes to the observed spectral differences, we analyzed pixel-resolved clustering results (Supplementary Fig. S1). While t-SNE reveals spatially heterogeneous regions within each tissue section, the corresponding cluster-averaged spectra exhibit highly consistent spectral profiles with variations primarily in absorbance intensity rather than peak positions or shapes. This indicates that intra-ROI heterogeneity is dominated by local intensity variations rather than intrinsic biochemical differences. Therefore, the preparation-dependent spectral differences reported in this study cannot be attributed to thickness or spatial variability alone, but instead reflect genuine biochemical alterations induced by FFPE processing.

View Article Online
DOI: 10.1039/D6AN00137H

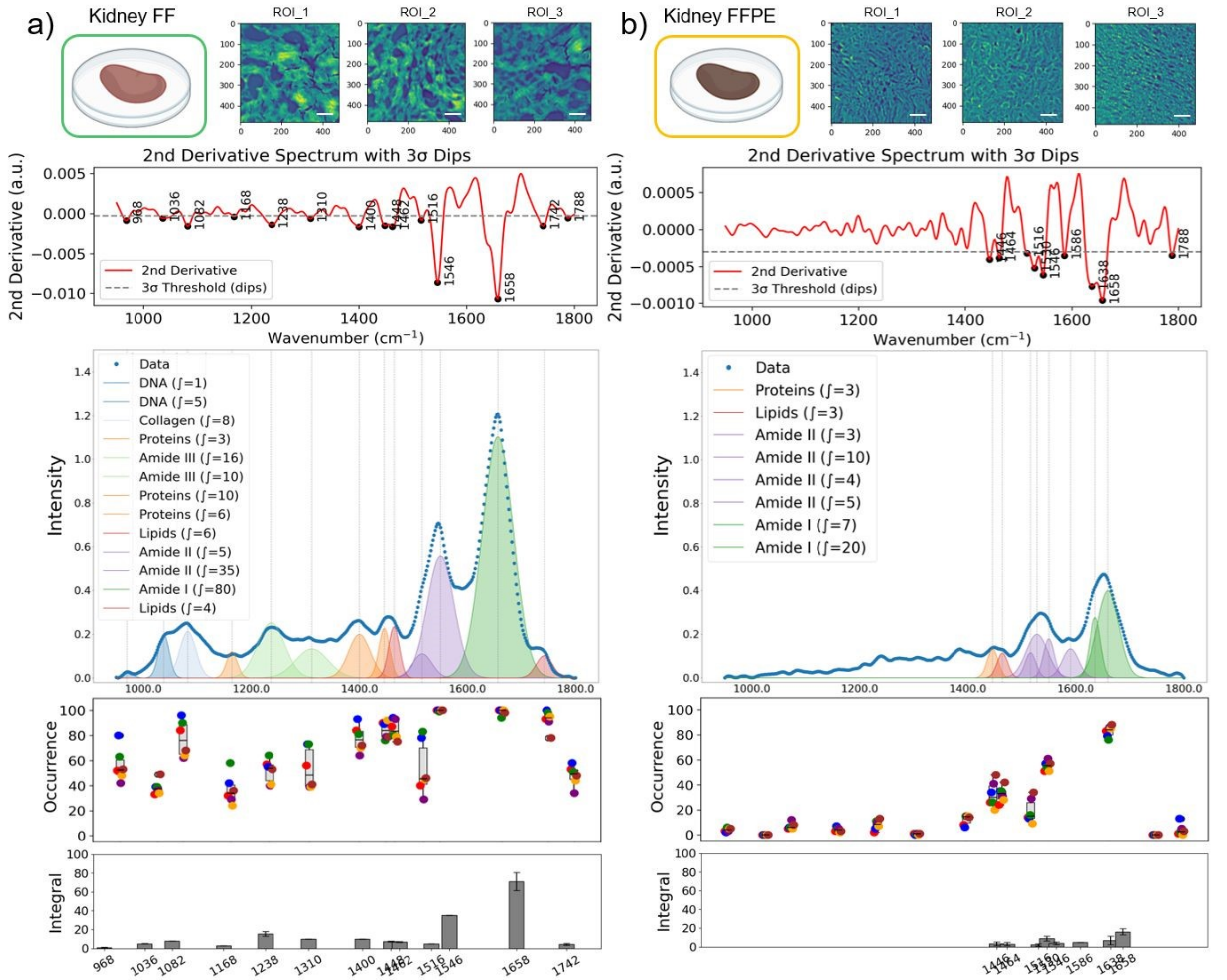

***Figure 3**. **Comparative spectral data variations in kidney FF and FFPE tissues.** Three representative mid-infrared images (ROIs) captured at the Amide I band (1608 cm^{-1}) are shown for kidney FF (a) and FFPE (b) tissues. Scale bars indicate 100 μm. Second-derivative spectra with dips detected by the 3-sigma rule. The intensity plots show the average mid-infrared spectra generated by randomly selected 120 pixel-spectra from eight ROIs, and the sub-bands were identified by second-derivative analysis, and Gaussian fitting was applied for FF (a) and FFPE (b) tissues. The occurrence of the detected absorbance peaks from eight ROIs was plotted (each ROI was represented by 100 pixels) for FF (a) and FFPE (b) tissues. Each data point represents the average occurrence from a single ROI; the grey box-and-whisker plot shows the center and spread of the peak occurrence. In the bottom integral plots, the dark grey bars represent the average and standard deviation of the integral calculated for each specific band.*

Similarly, FF liver tissues showed more diverse and stronger molecular signatures across the spectral range compared to FFPE tissue sections (Figure 4). While Amide I and II bands, which are typically strong, remained detectable in FFPE liver tissues, multiple bands below 1400 cm⁻¹ were lost. This observation indicates that FFPE processing does not simply attenuate the spectrum uniformly, but preferentially suppresses or alters specific biochemical features, particularly in the lower-wavenumber fingerprint region. Considering spectral data from eight ROIs (100 spectra per ROI) per FF and FFPE samples, we consistently identified thirteen distinct peaks in FF liver tissues, while only seven peaks were captured across different pixel spectra in FFPE samples. The occurrence of significant peaks was presented for FF and FFPE in Figure 4a and b, respectively, summarizing the diversity of bands captured from different ROIs. While some variability across ROIs is observed, Supplementary Fig. S1 demonstrates that these

View Article Online
DOI: 10.1039/D6AN00137H

differences are primarily driven by variations in absorbance intensity rather than changes in spectral profiles. We also identified that the average absorbance of the Amide 1 band in FFPE was 46.2% lower than the FF liver tissue measurements, in alignment with our findings with kidney tissue.

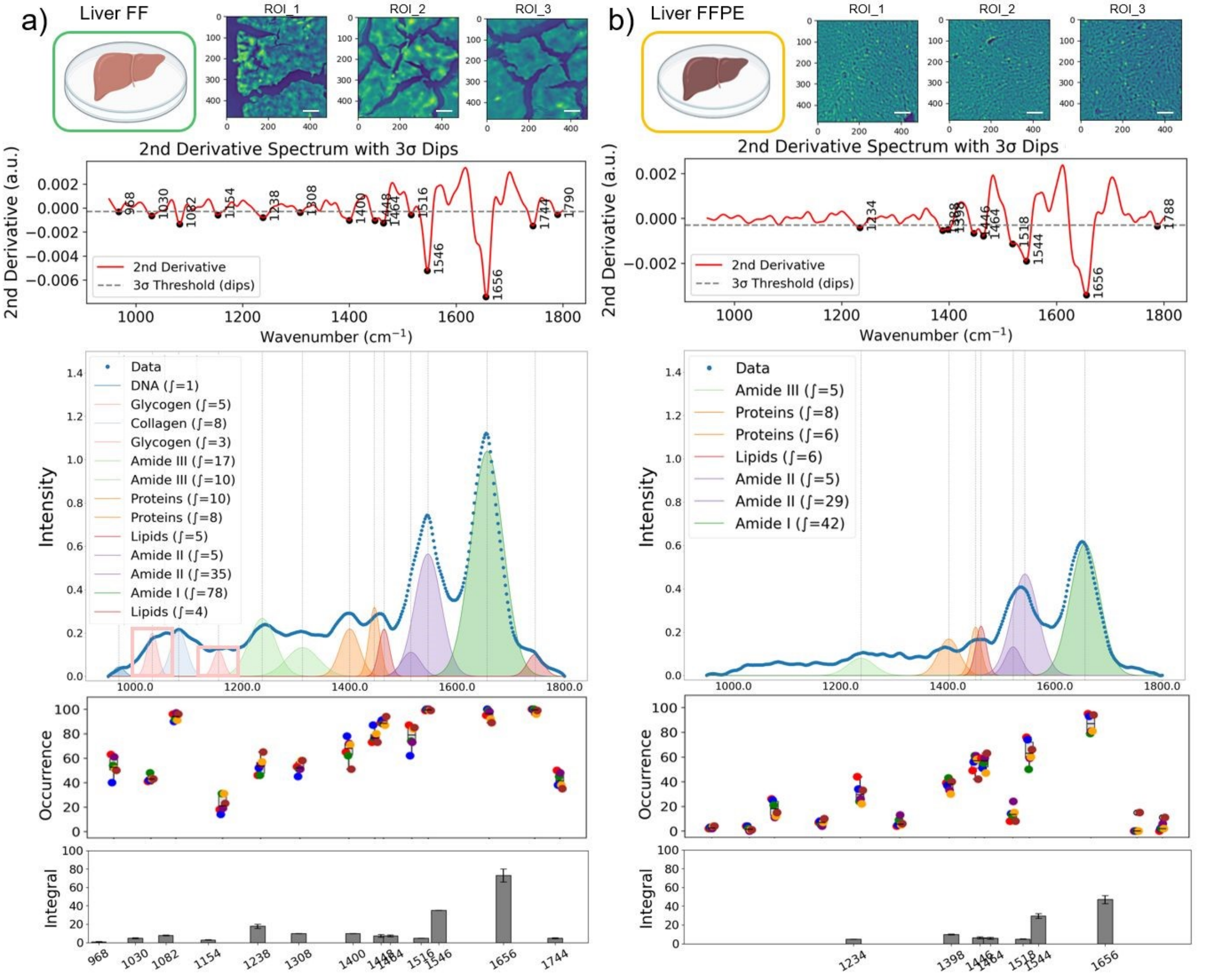

***Figure 4*. Comparative spectral data variations in liver FF and FFPE tissues.** *Three representative mid-infrared images captured at the Amide I band (1608 cm^{-1}) are shown for liver FF (a) and FFPE (b) tissues. Scale bars indicate 100 μm. Second-derivative spectra with dips detected by the 3-sigma rule. The intensity plots show average mid-infrared spectra generated by randomly selected 120 pixel-spectra from eight ROIs, and the sub-bands were identified by second-derivative analysis, and Gaussian fitting was applied for FF (a) and FFPE (b) tissues. The occurrence of the detected absorbance peaks from eight ROIs was plotted (each ROI was represented by 100 pixels) for FF (a) and FFPE (b) tissues. Each data point represents the average occurrence from a single ROI; the grey box-and-whisker plot shows the center and spread of the data. In the bottom integral plots, the dark grey bars represent the average and standard deviation of the integral calculated for each specific band.*

Liver is an organ with a high metabolic complexity and an abundance of chemically labile molecules. The reduction in spectral intensity and band loss in FFPE samples can be attributed to the chemical consequences of formalin fixation, including protein crosslinking as well as removal of lipophilic and labile components during dehydration in ethanol and paraffin embedding. For example, the glycogen band (@1030cm^{-1}), a marker of hepatic metabolism[41], was only observed in FF liver tissues (as highlighted in Figure 4a). Collectively, these findings

View Article Online
DOI: 10.1039/D6AN00137H

underscore the limitations of FFPE for comprehensive chemical mapping and highlight the advantages of FF preparation in preserving the biochemical complexity of metabolically active tissues for MIRSI analysis.

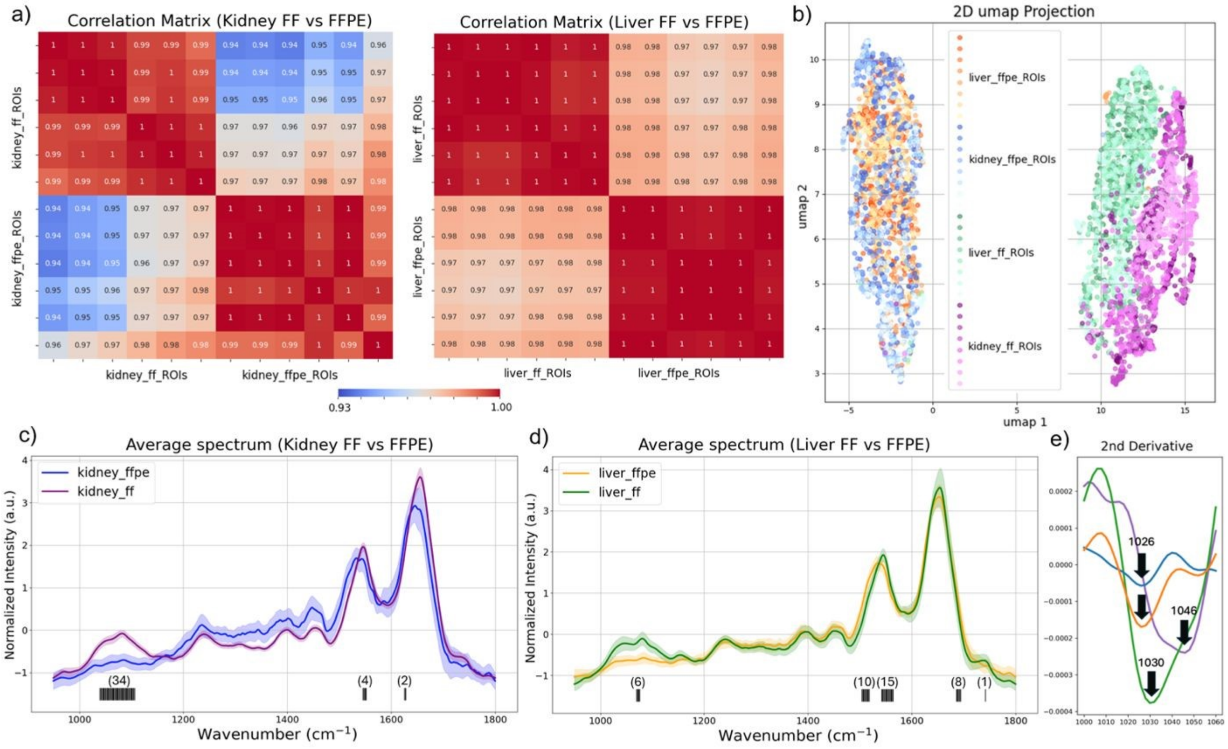

Figure 5. Correlation matrices and UMAP clustering reveal tissue processing effects on the spectral discrimination power in chemical imaging. *a). Correlation heatmaps demonstrate the degree of spectral similarity within ROIs of the same sample type and highlight differences across tissues prepared using different protocols. b) UMAP projection of normalized spectra from FF and FFPE rat kidney and liver tissues. c) Averaged and normalized spectra from liver FF and FFPE samples were plotted and top 40 discriminative wavenumbers were identified and indicated as the black lines under the spectra. d) Averaged and normalized spectra from kidney FF and FFPE samples were plotted and top 40 discriminative wavenumbers were identified and indicated as the black lines under the spectra. Number in the parentheses indicate the number of important features detected. e) Zoom-in second derivative spectra from 1000 cm^{-1} to 1060 cm^{-1} showing the distinct absorption band at 1026 cm^{-1} detected dominantly in FFPE samples.*

U-map and Feature Importance Analysis of Spectral Profiles

To further investigate the impact of sample preparation on the discriminatory power of spectral features, we first calculated correlation matrices between ROIs from different sample types and displayed them as a heatmap (Figure 5a). The correlation matrices illustrate a high degree of similarity in spectra from different ROIs of the same sample type, while highlighting differences due to tissue processing for both liver and kidney tissues.

Moreover, we applied UMAP to preprocessed spectra from rat kidney and liver tissues. A total of 20,000 spectra were used for UMAP after reducing spectral dimensionality using PCA. From a total of eight ROIs, 5000 spectra were randomly selected from each sample type (FF and FFPE liver and kidney). UMAP revealed distinct clustering patterns based on the tissue processing method. Independent of tissue type, liver or kidney, spectra from FFPE-processed samples formed a single, tightly grouped cluster. On the contrary, spectra from FF samples retained distinct spectral features between kidney and liver tissues (Figure 5b). Given that the considered

View Article Online
DOI: 10.1039/D6AN00137H

organs, the liver and kidney, have distinct biological and physiological functionalities, the discrimination between their chemical composition captured by the FF tissue spectra is expected. On the contrary, the overlapping UMAP clusters among the FFPE tissue spectra indicate that the chemically intrusive sample processing removes the key spectral features unique to each organ type.

To identify the most discriminative spectral features, we applied a logistic regression model to the UMAP-clustered spectral datasets and identified the highest-ranked feature importance wavenumbers across kidney and liver samples. The top 40 contributing wavenumbers were predominantly located in the lower wavenumber region (nucleic acids bands, carbohydrate-associated bands), as well as the Amide I and II regions, which are the key vibrational modes linked to functional biomolecules (Figure 5c, d). This result further indicates that the differences between FF and FFPE tissues are not solely driven by global amplitude attenuation, but also by subtle, preparation-dependent changes in the relative spectral structure of the fingerprint and amide regions. These results highlight the superior spectral fidelity of FF tissues in preserving biologically relevant features, which are essential to apply chemical imaging for biomedical research and diagnostic applications.

Additional Spectral Feature in FFPE Tissues

In addition to signal attenuation, FFPE processing introduced a distinct absorption band at ~1026 cm^{-1} that was not observed in any fresh-frozen (FF) samples (Figure 5e). This feature was consistently detected in FFPE liver sections and partially in kidney, indicating that it is associated with fixation rather than intrinsic tissue composition.

Rather than assigning this band to a specific chemical group, we interpret it as a fixation-related spectral feature. Formaldehyde fixation is known to involve multistep reactions, including the formation of reversible methylol ($-CH_2OH$) adducts followed by condensation into more stable crosslinked structures such as methylene bridges[14]. Prior studies using model peptides and mass spectrometry have demonstrated that these reactions generate a heterogeneous ensemble of modified protein species rather than a single dominant product[42,43]. In this context, the ~1026 cm^{-1} band may plausibly reflect vibrational contributions associated with fixation-induced chemical modifications and/or structural rearrangements, although a definitive assignment cannot be made.

Importantly, beyond the emergence of this additional feature, we also observe systematic spectral shifts in the Amide I and Amide II regions (Figure 5c,d). Such band shifts have been widely reported in vibrational spectroscopic studies of formalin-fixed tissues and are generally attributed to changes in protein conformation, hydrogen bonding, and molecular environment induced by crosslinking[44-47]. The presence of these shifts in our data further supports that FFPE processing induces measurable biochemical and structural alterations.

Together, these results indicate that FFPE preparation not only reduces native spectral contrast but also introduces fixation-related spectral features. These effects should be carefully considered when interpreting spectroscopic data in studies aimed at probing intrinsic biochemical signatures.

View Article Online
DOI: 10.1039/D6AN00137H

Implications for Chemical Imaging-Based Tissue Analysis

Complementary insights from Raman spectroscopy (RS) further support the interpretation of preparation-induced spectral changes observed in this study. Previous RS-based investigations comparing fresh and FFPE tissues have shown that formalin fixation generally preserves the dominant biochemical signatures while introducing measurable variations, including intensity changes and band shifts associated with protein crosslinking and alterations in molecular conformation[44-46].

These observations are consistent with our MIRSI findings, where major spectral features remain conserved across preparation methods, while fixation induces reduced spectral diversity and the emergence of preparation-specific features. Together, our findings highlight the important role of sample preparation protocols on the fidelity and interpretability of spectrochemical tissue image datasets. While FFPE is widely used for its morphological preservation and long-term storage benefits, the harsh chemical treatments involved can compromise labile molecular signatures and introduce fixation-specific artifacts, limiting analytical depth and complicating AI-based classification or biomarker discovery pipelines.

In contrast, FF preparation, though more logistically demanding, preserves both biologically and physiologically informative molecular signatures. However, as the mid-IR images show, the tissue morphology is hindered in FF sections. This is not a significant hurdle because morphology can be easily analyzed using well-established histopathology techniques using accessible optical widefield microscopes. As MIRSI applications continue to expand in biomedical research, careful consideration of sample preparation protocols will be essential to maintain the innate chemical composition, which can enable accurate spectral classification and support robust machine learning applications.

Our results suggest that sample preparation strategies should be carefully selected based on the primary objective of the imaging study. Fresh frozen (FF) tissues are preferable when preserving biochemical fidelity is critical, as they better retain native molecular composition and spectral diversity. In contrast, FFPE tissues provide superior morphological preservation and long-term stability but may introduce fixation-induced spectral features, which can reduce spectral variability and obscure subtle biochemical features.

Importantly, we note that optimal preparation conditions are tissue-dependent. Variations in tissue composition (e.g., lipid-rich vs. protein-rich tissues) can significantly influence both fixation efficiency and spectral outcomes. Therefore, optimization of FF tissue preparation and mounting protocols, such as minimizing freeze–thaw cycles, controlling sectioning temperature, and ensuring consistent substrate contact is critical to preserve both structural integrity and spectral quality. Notably, chemical imaging studies can benefit from more recent FF tissue preparation methods with advanced molecular preservation.[48] For FFPE samples, we recommend strict standardization of fixation duration, paraffin processing, and solvent-based dewaxing steps, as these parameters can significantly affect spectral reproducibility. Prior studies have also highlighted that differences in fixation time, dehydration protocols, and dewaxing efficiency can lead to measurable spectral variations emphasizing the need for controlled and consistent workflows[49-50].

View Article Online
DOI: 10.1039/D6AN00137H

Conclusion

This study demonstrates that tissue sample processing significantly affects the preservation of biochemical information in mid-IR spectrochemical imaging. By directly comparing mid-IR spectra from FF and FFPE rat kidney and liver tissues, we show that FF samples consistently preserved a more diverse and intense range of biochemical signals, compared to that of FFPE tissues. Notably, we observed a consistent spectral band at 1026 cm^{-1} primarily in FFPE samples, likely arising from fixation-induced chemical modifications and/or structural rearrangements. These findings highlight that FFPE processing not only diminishes native molecular signatures but can also introduce fixation-specific artifacts. As chemical imaging advances toward clinical and AI-integrated biomedical applications, optimizing and standardizing sample preparation across the chemical imaging research community will be essential to ensure spectral fidelity and accurate biochemical interpretation.

Acknowledgement

The authors thank the University of Wisconsin Translational Research Initiatives in Pathology (TRIP) Laboratory, supported by the UW Department of Pathology and Laboratory Medicine, UWCCC (P30 CA014520), and the Office of the Director- NIH (S10 OD023526) for use of its facilities and histology services. F.Y. and P.C. acknowledge financial support from the U.S. National Institutes of Health (R61CA281795).

Data Availability

The data that support the findings of this study are available from the corresponding author upon reasonable request. All code used for spectral processing, analysis, and visualization is openly available on GitHub at: https://github.com/YesilkoyLab/public-.git

Reference

1. Wrobel, T. P.; Bhargava, R. Infrared Spectroscopic Imaging Advances as an Analytical Technology for Biomedical Sciences. *Anal. Chem.* **2018**, *90* (3), 1444–1463. https://doi.org/10.1021/acs.analchem.7b05330.
2. Fernandez, D. C.; Bhargava, R.; Hewitt, S. M.; Levin, I. W. Infrared Spectroscopic Imaging for Histopathologic Recognition. *Nat. Biotechnol.* **2005**, *23* (4), 469–474. https://doi.org/10.1038/nbt1080.
3. Paraskevaidi, M.; Matthew, B. J.; Holly, B. J.; Hugh, B. J.; Thulya, C. P. V.; Loren, C.; St John, C.; Peter, G.; Callum, G.; Sergei, K. G.; Kamila, K.; Maria, K.; Kássio, L. M. G.; Pierre, M.-H. L.; Evangelos, P.; Savithri, P.; John, A. A.; Alexandra, S.; Marfran, S.; Josep, S.-S.; Gunjan, T.; Michael, W.; Bayden, W. Clinical Applications of Infrared and Raman Spectroscopy in the Fields of Cancer and Infectious Diseases. *Appl. Spectrosc. Rev.* **2021**, *56* (8–10), 804–868. https://doi.org/10.1080/05704928.2021.1946076.
4. Baker, M. J.; Trevisan, J.; Bassan, P.; Bhargava, R.; Butler, H. J.; Dorling, K. M.; Fielden, P. R.; Fogarty, S. W.; Fullwood, N. J.; Heys, K. A.; Hughes, C.; Lasch, P.; Martin-Hirsch, P. L.; Obinaju, B.; Sockalingum, G. D.; Sulé-Suso, J.; Strong, R. J.; Walsh, M. J.; Wood, B. R.; Gardner, P.; Martin, F. L. Using Fourier Transform IR Spectroscopy to Analyze Biological Materials. *Nat. Protoc.* **2014**, *9* (8), 1771–1791. https://doi.org/10.1038/nprot.2014.110.

View Article Online
DOI: 10.1039/D6AN00137H

5. Al-Kelani, M.; Buthelezi, N. Advancements in Medical Research: Exploring Fourier Transform Infrared (FTIR) Spectroscopy for Tissue, Cell, and Hair Sample Analysis. *Skin Res. Technol.* **2024**, *30* (6), e13733. https://doi.org/10.1111/srt.13733.
6. Chang, P.; Ishrak, R.; Hoghooghi, N.; Egbert, S.; Lesko, D.; Swartz, S.; Biegert, J.; Rieker, G. B.; Reddy, R.; Diddams, S. A. Mid-Infrared Hyperspectral Microscopy with Broadband 1 GHz Dual Frequency Combs. *APL Photonics* **2024**, *9* (10), 106111. https://doi.org/10.1063/5.0225616.
7. Kole, M. R.; Reddy, R. K.; Schulmerich, M. V.; Gelber, M. K.; Bhargava, R. Discrete Frequency Infrared Microspectroscopy and Imaging with a Tunable Quantum Cascade Laser. *Anal. Chem.* **2012**, *84* (23), 10366–10372. https://doi.org/10.1021/ac302513f.
8. Yeh, K.; Sharma, I.; Falahkheirkhah, K.; Confer, M. P.; Orr, A. C.; Liu, Y.-T.; Phal, Y.; Ho, R.-J.; Mehta, M.; Bhargava, A.; Mei, W.; Cheng, G.; Cheville, J. C.; Bhargava, R. Infrared Spectroscopic Laser Scanning Confocal Microscopy for Whole-Slide Chemical Imaging. *Nat. Commun.* **2023**, *14* (1), 5215. https://doi.org/10.1038/s41467-023-40740-w.
9. Zhang, D.; Li, C.; Zhang, C.; Slipchenko, M. N.; Eakins, G.; Cheng, J.-X. Depth-Resolved Mid-Infrared Photothermal Imaging of Living Cells and Organisms with Submicrometer Spatial Resolution. *Sci. Adv.* **2016**, *2* (9), e1600521. https://doi.org/10.1126/sciadv.1600521.
10. Tiwari, S.; Kajdacsy-Balla, A.; Whiteley, J.; Cheng, G.; Jirstrom, K.; Birgisson, H.; Hewitt, S. M.; Bhargava, R. INFORM: Infrared-Based Organizational Measurements of Tumor and Its Microenvironment to Predict Patient Survival. *Sci. Adv.* **2021**, *7* (6), eabb8292. https://doi.org/10.1126/sciadv.abb8292.
11. Bhargava, R. Digital Histopathology by Infrared Spectroscopic Imaging. *Annu. Rev. Anal. Chem.* **2023**, *16*, 205–230. https://doi.org/10.1146/annurev-anchem-101422-090956.
12. Old, O. J.; Fullwood, L. M.; Scott, R.; Lloyd, G. R.; Almond, L. M.; Shepherd, N. A.; Stone, N.; Barr, H.; Kendall, C. Vibrational Spectroscopy for Cancer Diagnostics. *Anal. Methods* **2014**, *6* (12), 3901–3917. https://doi.org/10.1039/C3AY42235F.
13. Sharma, V. J.; Singh, A.; Grant, J. L.; Raman, J. Point-of-Care Diagnosis of Tissue Fibrosis: A Review of Advances in Vibrational Spectroscopy with Machine Learning. *Pathology* **2024**, *56* (3), 313–321. https://doi.org/10.1016/j.pathol.2023.11.008.
14. Fox, C. H.; Johnson, F. B.; Whiting, J.; Roller, P. P. Formaldehyde Fixation. *J. Histochem. Cytochem.* **1985**, *33* (8), 845–853. https://doi.org/10.1177/33.8.3894502.
15. Bass, B. P.; Engel, K. B.; Greytak, S. R.; Moore, H. M. A Review of Preanalytical Factors Affecting Molecular, Protein, and Morphological Analysis of FFPE Tissue. *Arch. Pathol. Lab. Med.* **2014**, *138* (11), 1520–1530. https://doi.org/10.5858/arpa.2013-0691-RA.
16. Groelz, D.; Viertler, C.; Pabst, D.; Dettmann, N.; Zatloukal, K. Impact of Storage Conditions on the Quality of Nucleic Acids in Paraffin-Embedded Tissues. *PLoS One* **2018**, *13* (9), e0203608. https://doi.org/10.1371/journal.pone.0203608.
17. Shabihkhani, M.; Lucey, G. M.; Wei, B.; Mareninov, S.; Lou, J. J.; Vinters, H. V.; Singer, E. J.; Cloughesy, T. F.; Yong, W. H. The Procurement, Storage, and Quality Assurance of Frozen Biospecimens. *Clin. Biochem.* **2014**, *47* (4–5), 258–266. https://doi.org/10.1016/j.clinbiochem.2014.01.002.

View Article Online
DOI: 10.1039/D6AN00137H

18. Stec, P.; et al. Fourier Transform Infrared Microspectroscopy Analysis of Ovarian Cancer Tissues. *Spectrochim. Acta A* **2023**, *297*, 122717. https://doi.org/10.1016/j.saa.2023.122717.
19. Stefanakis, M.; et al. Impact of Tissue Preparation on Salivary Gland Tumors. *J. Clin. Med.* **2023**, *12* (2), 569. https://doi.org/10.3390/jcm12020569.
20. Verdonck, M.; et al. Breast Cancer Identification by FTIR Imaging after FFPE. *Analyst* **2013**, *138* (14), 4083–4091. https://doi.org/10.1039/c3an00246b.
21. Ning, T.; Li, H.; Chen, Y.; Zhang, B.; Zhang, F.; Wang, S. Raman Spectroscopy Analysis of FFPE Breast Cancer Tissue. *Vib. Spectrosc.* **2021**, *115*, 103260. https://doi.org/10.1016/j.vibspec.2021.103260.
22. Li, R.; Allen, H. C. Developing Transferable IR Biomarkers. *Sci. Rep.* **2025**, *15*, 22944. https://doi.org/10.1038/s41598-025-05068-z.
23. Rosas, S.; Schoeller, K. A.; Chang, E.; Mei, H.; Kats, M. A.; Eliceiri, K. W.; Zhao, X.; Yesilkoy, F. Metasurface-Enhanced Mid-Infrared Imaging. *Adv. Mater.* **2023**, *35*, 2301208. https://doi.org/10.1002/adma.202301208.
24. Sezgin, M.; Sankur, B. Survey over Image Thresholding Techniques and Quantitative Performance Evaluation. *J. Electron. Imaging* **2004**, *13* (1), 146–165. https://doi.org/10.1117/1.1631315.
25. Bassan, P.; Byrne, H. J.; Bonnier, F.; Lee, J.; Dumas, P.; Gardner, P. Resonant Mie Scattering in Infrared Spectroscopy of Biological Materials: Understanding the Dispersion Artefact. *Analyst* **2009**, *134* (8), 1586–1593. https://doi.org/10.1039/B904808A.
26. Savitzky, A.; Golay, M. J. E. Smoothing and Differentiation of Data by Simplified Least Squares Procedures. *Anal. Chem.* **1964**, *36* (8), 1627–1639. https://doi.org/10.1021/ac60214a047.
27. Fratini, S. *Mathematical Thinking: Exercises for the Mind*; Springer: Cham, 2020.
28. Movasaghi, Z.; Rehman, S.; Rehman, I. U. Fourier Transform Infrared (FTIR) Spectroscopy of Biological Tissues. *Appl. Spectrosc. Rev.* **2008**, *43* (2), 134–179. https://doi.org/10.1080/05704920701829043.
29. Fung, M. F. K.; Senterman, M. K.; Mikhael, N. Z.; Lacelle, S.; Wong, P. T. T. Pressure-Tuning Fourier Transform Infrared Spectroscopic Study of Carcinogenesis in Human Endometrium. *Biospectroscopy* **1996**, *2*, 155–165.
30. Wang, H. P.; Wang, H.-C.; Huang, Y.-J. Microscopic FTIR Studies of Lung Cancer Cells in Pleural Fluid. *Sci. Total Environ.* **1997**, *204*, 283–287.
31. Gazi, E.; Dwyer, J.; Gardner, P.; Ghanbari-Siakhani, A.; Wade, A. P.; Lockyer, N. P.; Vickerman, J. C.; Clarke, N. W.; Shanks, J. H.; Scott, L. J.; Hart, C. A.; Brown, M. Applications of Fourier Transform Infrared Microspectroscopy in Studies of Benign Prostate and Prostate Cancer: A Pilot Study. *J. Pathol.* **2003**, *201*, 99–108.
32. Huleihel, M.; Salman, A.; Erukhimovich, V.; Ramesh, J.; Hammody, Z.; Mordechai, S. Novel Optical Method for Study of Viral Carcinogenesis in Vitro. *J. Biochem. Biophys. Methods* **2002**, *50*, 111–121.
33. Yano, K.; Ohoshima, S.; Grotou, Y.; Kumaido, K.; Moriguchi, T.; Katayama, H. Direct Measurement of Human Lung Cancerous and Noncancerous Tissues by Fourier Transform Infrared Microscopy. *Anal. Biochem.* **2000**, *287*, 218–225.

View Article Online
DOI: 10.1039/D6AN00137H

34. Chiriboga, L.; Xie, P.; Yee, H.; Vigorita, V.; Zarou, D.; Zakim, D.; Diem, M. Infrared Spectroscopy of Human Tissue. I. Differentiation and Maturation of Epithelial Cells in the Human Cervix. *Biospectroscopy* **1998**, *4*, 47–53.
35. Fukuyama, Y.; Yoshida, S.; Yanagisawa, S.; Shimizu, M. Differences between Oral Squamous Cell Carcinomas and Normal Oral Mucosas Measured by FTIR Spectroscopy. *Biospectroscopy* **1999**, *5*, 117–126.
36. Fabian, H.; Jackson, M.; Murphy, L.; Watson, P. H.; Fichtner, I.; Mantsch, H. H. Comparative Infrared Spectroscopic Study of Human Breast Tumors and Tumor Cell Xenografts. *Biospectroscopy* **1995**, *1* (1), 37–45.
37. Richter, T.; Steiner, G.; Abu-Id, M. H.; Salzer, R.; Bergmann, R.; Rödig, H.; Johannsen, B. Identification of Tumor Tissue by FTIR Spectroscopy in Combination with PET. *Vib. Spectrosc.* **2002**, *28*, 103–110.
38. Argov, S.; Sahu, R. K.; Bernshtain, E.; Salam, A.; Shohat, G.; Zelig, U.; Mordechai, S. Inflammatory Bowel Diseases as an Intermediate Stage between Normal and Cancer. *Biopolymers* **2004**, *75*, 384–392.
39. Shetty, G.; Kendall, C.; Shepherd, N.; Stone, N.; Barr, H. Raman Spectroscopy: Evaluation of Biochemical Changes in Carcinogenesis of Oesophagus. *Br. J. Cancer* **2006**, *94*, 1460–1464.
40. Eckel, R.; Huo, H.; Guan, H.-W.; Hu, X.; Che, X.; Huang, W.-D. Characteristic Infrared Spectroscopic Patterns in Protein Bands of Human Breast Cancer Tissue. *Vib. Spectrosc.* **2001**, *27*, 165–173.
41. Adeva-Andany, M. M.; et al. Glycogen Metabolism in Humans. *BBA Clin.* **2016**, *5*, 85–100. https://doi.org/10.1016/j.bbacli.2016.02.001.
42. Metz, B.; Kersten, G. F. A.; Hoogerhout, P.; Brugghe, H. F.; Timmermans, H. A. M.; de Jong, A.; Meiring, H.; ten Hove, J.; Hennink, W. E.; Crommelin, D. J. A.; Jiskoot, W. Identification of Formaldehyde-Induced Modifications in Proteins. *J. Biol. Chem.* **2004**, *279* (8), 6235–6243. https://doi.org/10.1074/jbc.M310752200.
43. Toews, J.; Rogalski, J. C.; Clark, T. J.; Kast, J. Mass Spectrometric Identification of Formaldehyde-Induced Peptide Modifications. *Anal. Chim. Acta* **2008**, *618* (2), 168–183. https://doi.org/10.1016/j.aca.2008.04.049.
44. Lyng, F.; Gazi, E. Preparation of Tissues and Cells for Infrared and Raman Spectroscopy and Imaging. In *Biomedical Applications of Synchrotron Infrared Microspectroscopy*; Wiley, 2011.
45. Huang, Z.; McWilliams, A.; Lam, S.; English, J.; McLean, D. I.; Lui, H.; Zeng, H. Effect of Formalin Fixation on Near-Infrared Raman Spectroscopy of Bronchial Tissues. *Int. J. Oncol.* **2003**, *23* (3), 649–655.
46. Tfayli, A.; Gobinet, C.; Vrabie, V.; Huez, R.; Manfait, M.; Piot, O. Digital Dewaxing of Raman Signals from Paraffin-Embedded Biopsies. *Appl. Spectrosc.* **2009**, *63* (5), 564–570. https://doi.org/10.1366/000370209788347048.
47. Lita, A.; Sjöberg, J.; Păcioianu, D.; Siminea, N.; Celiku, O.; Dowdy, T.; Păun, A.; Gilbert, M. R.; Noushmehr, H.; Petre, I.; Larion, M. Raman-Based Machine Learning for Glioma Metabolic Differences. *Neuro-Oncology* **2024**, *26* (11), 1994–2009. https://doi.org/10.1093/neuonc/noae101.
48. Dannhorn, A.; Kazanc, E.; Flint, L.; et al. Morphological and Molecular Preservation through Universal Preparation of Fresh-Frozen Tissue Samples. *Nat. Protoc.* **2024**, *19*, 2685–2711. https://doi.org/10.1038/s41596-024-00987-z.

View Article Online
DOI: 10.1039/D6AN00137H

49. Faoláin, E. Ó.; Hunter, M. B.; Byrne, J. M.; Kelehan, P.; Lambkin, H. A.; Byrne, H. J.; Lyng, F. M. Raman Spectroscopic Evaluation of Paraffin Wax Dewaxing Agents. *J. Histochem. Cytochem.* **2005**, *53* (1), 121–129. https://doi.org/10.1177/002215540505300114.
50. Knoblich, M.; Bassler, M.; Walczuch, T.; Hartmann, E.; Youssef, A.; Scherzad, A.; Stoeth, M.; Ostertag, E.; Hagen, R.; Steinke, M.; Hackenberg, S.; Brecht, M.; Meyer, T. Impact of Tissue Preparation on Salivary Gland Tumors Investigated by FTIR Microspectroscopy. *J. Clin. Med.* **2023**, *12*, 569. https://doi.org/10.3390/jcm12020569.

View Article Online
DOI: 10.1039/D6AN00137H

Data Availability

The data that support the findings of this study are available from the corresponding author upon reasonable request. All code used for spectral processing, analysis, and visualization is openly available on GitHub at: https://github.com/YesilkoyLab/public-.git